

Three-stage binarization of color document images based on discrete wavelet transform and generative adversarial networks

Yu-Shian Lin, Rui-Yang Ju, *Member, IEEE*, Chih-Chia Chen, Chun-Tse Chien, and Jen-Shiun Chiang, *Member, IEEE*

Abstract—The efficient segmentation of foreground text information from the background in degraded color document images is a critical challenge in the preservation of ancient manuscripts. The imperfect preservation of ancient manuscripts over time has led to various types of degradation, such as staining, yellowing, and ink seepage, significantly affecting image binarization results. This work proposes a three-stage method using Generative Adversarial Networks (GAN) for enhancing and binarizing degraded color document images through Discrete Wavelet Transform (DWT). Stage-1 involves applying DWT and retaining the Low-Low (LL) subband images for image enhancement. In Stage-2, the original input image is divided into four single-channel images (Red, Green, Blue, and Gray), and each is trained with independent adversarial networks to extract color foreground information. In Stage-3, the output image from Stage-2 and the original input image are used to train independent adversarial networks for document binarization, enabling the integration of global and local features. The experimental results demonstrate that our proposed method outperforms other classic and state-of-the-art (SOTA) methods on the Document Image Binarization Contest (DIBCO) datasets. We have released our implementation code at <https://github.com/abcpp12383/ThreeStageBinarization>.

Index Terms—semantic segmentation, discrete wavelet transform, handwritten document image binarization, document enhancement, handwriting text recognition, generative adversarial networks

I. INTRODUCTION

HISTORICAL analysis of human societies primarily relies on reconstructing and analyzing preserved ancient documents. Parchment manuscripts and paintings have predominantly served as the means of preserving crucial ancient documents throughout the evolution of human society. Analyzing preserved ancient documents presents challenges due to potential forms of interference and degradation, including paper yellowing, text fading, page contamination, and moisture damage.

Manuscript received xxx xxx, xxxx. This paper is an expanded paper from The Pacific Rim International Conferences on Artificial Intelligence (PRICAI) held on November 17-19, 2023 in Jakarta, Indonesia. Y. Lin and R. Ju contributed equally to this work. J. Chiang is the corresponding author. This work is supported by National Science and Technology Council of Taiwan, under Grant Number: NSTC 112-2221-E-032-037-MY2.

Y. Lin, C. Chen, C. Chien and J. Chiang are with the Department of Electrical and Computer Engineering, Tamkang University, No.151, Yingzhuang Rd., Tamsui Dist., New Taipei City, 251301 Taiwan (e-mail: abcpp12383@gmail.com; crystal88irene@gmail.com; popper0927@hotmail.com; jsken.chiang@gmail.com).

R. Ju is with the Graduate Institute of Networking and Multimedia, National Taiwan University, No. 1, Sec. 4, Roosevelt Rd., Taipei City, 106335 Taiwan (e-mail: jryjry1094791442@gmail.com).

Document image enhancement is one of the most important tasks in the reconstruction and analysis of ancient documents. It involves binarizing the document image to extract essential text information from the page. However, improving the image quality of degraded documents requires solving several problems, such as text degradation and bleed-through [1], [2], [3], [4]. However, traditional binarization methods struggle to extract text information from the background of degraded documents effectively, leading to incomplete removal of shadows, noise, or loss of text information.

With the development of deep learning techniques, neural networks have been applied to image binarization. Calvo-Zaragoza and Gallego [5] introduced a selectional auto-encoder approach, parsing the text through a trained network model, and binarizing it using threshold. Fully Convolutional Network (FCN) [6], [7] enables the generated images to maintain the same size as the input images, and the task of generating document binarization using FCN [8] is also included in the semantic segmentation task. Hsia *et al.* [9] employed an inverse adaptive directional lifting wavelet transform with global binarization to convert grayscale images into binary output results. However, most image binarization methods primarily address grayscale documents, targeting contaminated black and white scanned ancient documents as their default.

Considering that some scanned images of ancient documents are in color, we propose a novel generative adversarial network framework for enhancing and binarizing color degraded documents [10]. The proposed method consists of three stages. In Stage-1, we split the original input image into four different color single-channel images, and apply Discrete Wavelet Transform (DWT) to retain the Low-Low (LL) subband images and normalize them to achieve the image enhancement of the original image. In Stage-2, we train four independent adversarial networks with the four single-channel images to eliminate background information and extract color foreground details from local image patches. During Stage-3, the multiscale adversarial networks produce local and global prediction outputs for the document images, which are subsequently fused to obtain the final output.

To evaluate the performance of the proposed method for degraded document image binarization, we compare it with other methods using DIBCO datasets of 2011, 2013, 2014, 2016, 2017, and 2018 [11], [12], [13], [14], [15], [16].

The main contributions of this paper are as follows:

- Introducing a novel three-stage generative adversarial

networks method for enhancing and binarizing degraded color documents.

- By utilizing Discrete Wavelet Transform before training the generative adversarial networks, the model performance improves with a better balance between text detail extraction and background error suppression.
- The proposed method achieves the state-of-the-art performance on multiple benchmark datasets.

The rest of this paper is organized as follows: Section II describes the deep learning method for document image binarization. Section III introduces a novel three-stage generative adversarial networks method. Section IV presents the comparison experiment and the ablation study, and compares the performance of our method and other methods on several benchmark datasets. Finally, Section V discusses the conclusion and the future work of this paper.

II. RELATED WORK

In previous research focused on document image binarization, the field is broadly divided into two categories: traditional image processing methods and deep learning-based semantic segmentation techniques. However, traditional image processing binarization methods, such as global binarization [17] and local adaptive binarization [18], [19], relying on pixel-level local threshold values, are inadequate when dealing with documents affected by excessive interference or degradation.

With the development of deep learning technology, the convolutional neural network (CNN) framework [20], [21] has become the main backbone of computer vision tasks. Within computer vision, semantic segmentation [7] is one of the most important research directions, encompassing document image binarization. For instance, Tensmeyer *et al.* [8] employed pseudo-F-measure (p-FM) and F-measure (FM) loss during the training of FCN to apply the model to the document image binarization task. Ronneberger *et al.* [22] extended FCN, presenting the U-Net architecture, which captures contextual and spatial information through its distinctive U-shaped design. Inspired by this, Peng *et al.* [23] introduced an encoder-decoder architecture for document image binarization, where the decoder transforms the low-resolution representation to the original dimensions, resulting in the binarized image. Vo *et al.* [24] first applied hierarchical deep supervised network (DSN) to document image binarization and achieved the SOTA performance on several benchmark datasets. He *et al.* [25] proposed an iterative deep learning framework applied to document image binarization and the trained model achieved excellent performance.

In recent years, Generative Adversarial Networks (GANs) [26] have achieved exciting results [27], [28] in the generation of real-world images. Unlike GANs which generate output images from random noise, Isola *et al.* [29] proposed Pix2Pix GAN based on conditional GAN (cGAN) [30] for image-to-image translation. To ensure that the generated images are more realistic, Pix2Pix GAN employs generators for loss function optimization. Within the network architecture, the generator evaluates the minimized generated image against the target output image, quantifying the $L1$ loss between them.

Meanwhile, the discriminator assesses the credibility of the generated image, relying on the input image and the reference target image. This process is depicted by the subsequent equation:

$$\arg \min_G \max_D V(G, D) = \mathbb{E}_x[\log(1 - D(x, G(x)))] + \mathbb{E}_{x,y}[\log D(x, y)] + \lambda \mathbb{E}_{x,y}[\|y - G(x)\|_1] \quad (1)$$

where the input data distribution \mathbb{P}_x samples the input image x ; the ground truth image of the input image is y , and the hyperparameter to increase the model regularization effect is λ . Generator G generates the input image as the generated image $G(x)$. From Eq. (1), the loss function between the generated image and the ground truth image is $L1$ instead of $L2$, which is beneficial to reduce the blurring and ambiguity in the generation process.

Bhunia *et al.* [31] performed texture enhancement on the dataset and used cGAN [30] for image binarization. Inspired by Pix2Pix GAN [29], Zhao *et al.* [32] proposed a cascade generator structure for document image binarization based on Pix2Pix GAN to solve the problem of multi-scale information combination. De *et al.* [33] designed two discriminators to combine local and global information. Suh *et al.* [34] set up a two-stage generative adversarial network for image binarization using Patch GAN [29]. Nicolaou *et al.* [35] proposed the TorMentor image enhancement framework by adapting global image enhancement transformations to continuous local transformations using plasma fractals. Souibgui *et al.* [36] proposed a new encoder-decoder architecture based on visual converters for enhancing machine printed and handwritten document images. These methods keep breaking the SOTA performance on DIBCO datasets.

III. PROPOSED METHOD

A. Overall Network Architecture

The aim of this work is to enhance image quality in the context of degraded color documents and extract text information from these document images. Since the degradation of color document images is diverse and complex, which requires processing of images with different color channels, our proposed method divides the overall network architecture into three stages. In Stage-1, we retain the images of LL subband by applying DWT. These images serve as a foundation for Stage-2 and Stage-3, where it is employed to train as the ground truth image of the generator within the adversarial network framework. Stage-2 focuses on the elimination of background color noise and the extraction of color foreground information, while Stage-3 involves the fusion of local and global predictions to produce the final output. The three stages operate independently, and detailed explanations of the content of each stage can be found in Sections III-B, III-C, and III-D respectively.

B. Stage-1

This work employs four different generators to extract foreground color information from degraded document images while eliminating the background color. The input color image

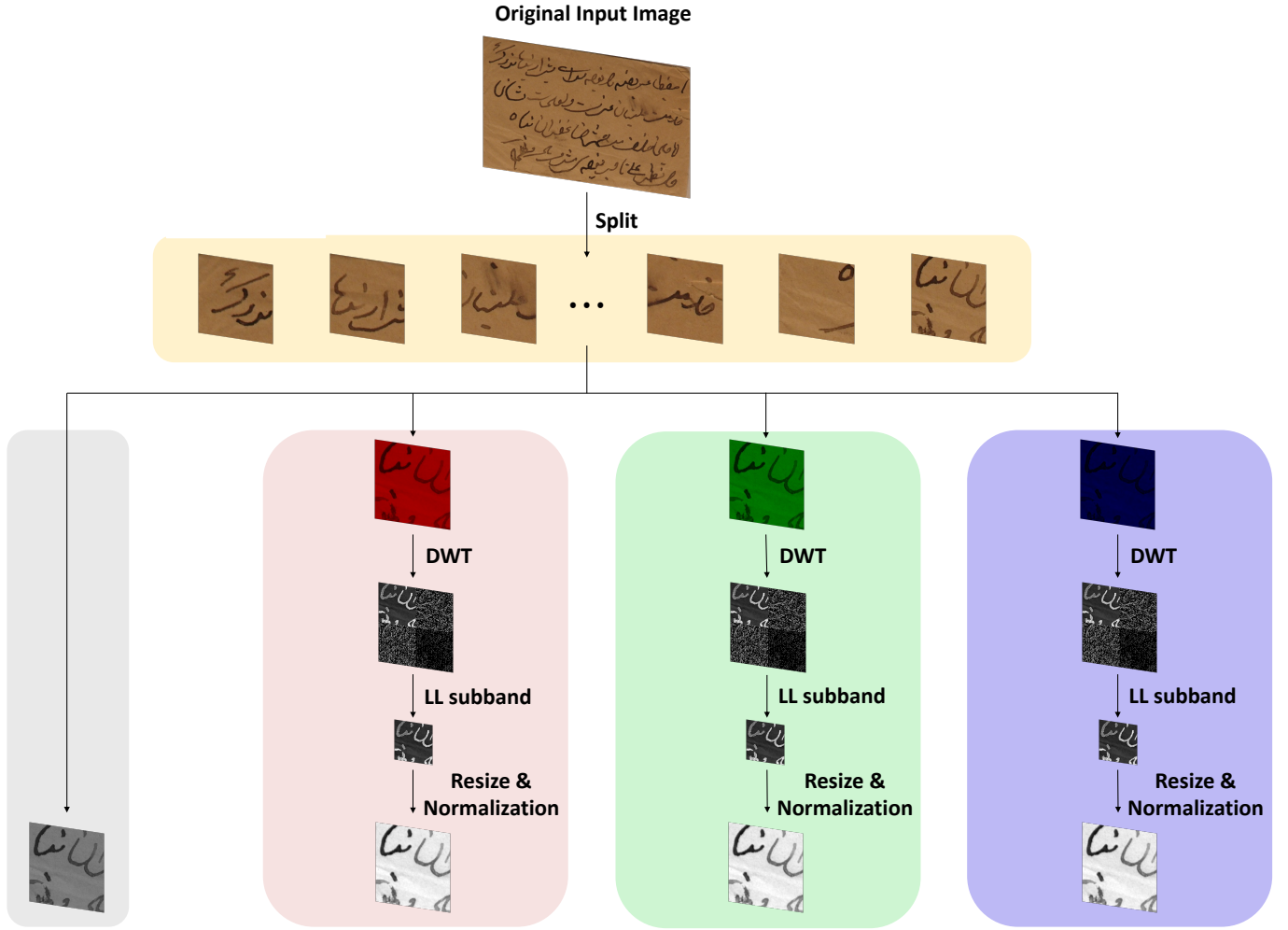


Fig. 1. The architecture diagram of the stage-1 of the proposed method. The original input image is divided into patches of 224×224 size, and split into four single-channel images (red, green, blue, and gray) for discrete wavelet transform and normalization.

is divided into four individual single-channel images: red, green, blue, and gray. The ground truth (GT) image provided by the dataset is a single-channel grayscale binary image, where pixel points have values of 0 for characters and 1 for the background. Images with varying channel numbers cannot be directly fed into the discriminator for processing. Therefore, we first split the three channels (red, green, blue) of the original input image to create three single-channel RGB images. Then we apply DWT to each RGB single-channel image, and retain the LL subband images for normalization. The ground truth images and the output images of Stage-1 are summed at pixel wise as the corresponding ground truth images of the generators in the RGB and gray channels. Fig. 1 illustrates the Stage-1 process, involving the initial division of the image into three single-channel RGB images, followed by the preservation of LL subband images and resizing to a designated size of 224×224 .

1) *Discrete Wavelet Transform*: The discrete wavelet transform (DWT) entails the inner product of the original image with both the wavelet basis function and the scale function. This process can be conceived as a bandpass filter, selec-

tively allowing signals with frequencies akin to those of the wavelet basis function to traverse. The flowchart of the DWT processing is illustrated in Fig. 2. Given single-channel split images as input, the initial step involves processing the n -direction through high pass, low pass, and frequency reduction operations. This results in an image comprising low-frequency composition on the left and high-frequency composition on the right. The equation for the one-dimensional DWT is shown below:

$$\begin{aligned} v_L[m, n] &= \sum_{k=0}^{K-1} x[m, 2n - k]g[k] \\ v_H[m, n] &= \sum_{k=0}^{K-1} x[m, 2n - k]h[k] \end{aligned} \quad (2)$$

High-pass, low-pass, and frequency reduction operations can be applied to Eq. 2) in the m -direction, resulting in the

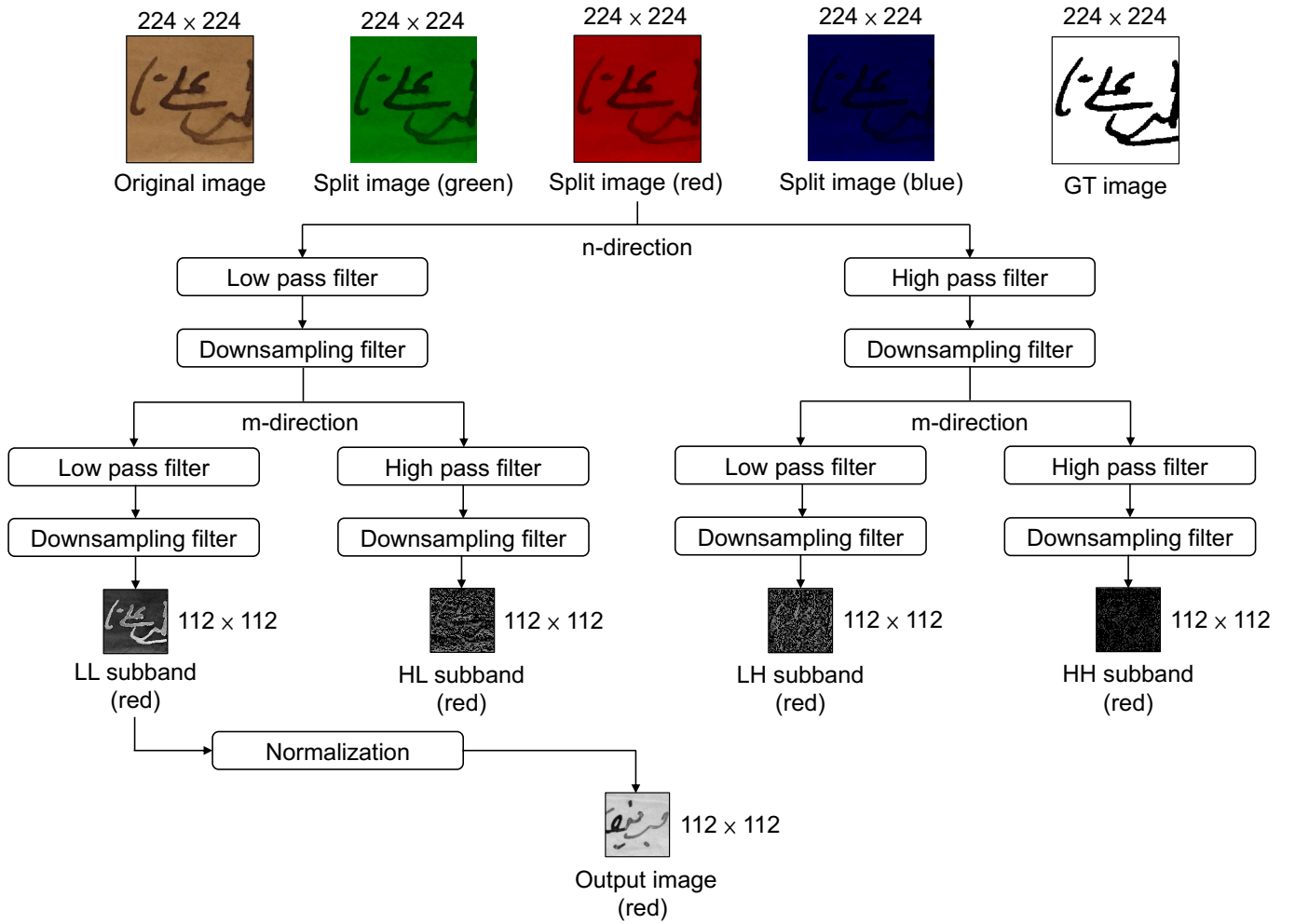


Fig. 2. The architecture diagram of the discrete wavelet transform used by the proposed method. The diagram takes the red single-channel image patch as an example, and the transform process of the green and blue single-channel image patch is the same.

following equations:

$$v_{LL}[m, n] = \sum_{k=0}^{K-1} v_L[2m - k, n]g[k] \quad (3)$$

$$v_{HL}[m, n] = \sum_{k=0}^{K-1} v_L[2m - k, n]h[k]$$

$$v_{LH}[m, n] = \sum_{k=0}^{K-1} v_H[2m - k, n]g[k] \quad (4)$$

$$v_{HH}[m, n] = \sum_{k=0}^{K-1} v_H[2m - k, n]h[k]$$

The application of the DWT generates four subband images: one low-frequency subband image and three high-frequency subband images. Specifically, the HL subband occupies the upper right corner, the LH subband is situated in the lower left corner, and the HH subband resides in the lower right corner.

In contrast to the ground truth images provided by the dataset, the three single-channel images generated from the original input images exhibit substantial noise. This noise

prevents their direct use in generating corresponding ground truth images through the generator and could potentially disrupt the performance of the trained adversarial network. The DWT decomposes the image into both low-frequency and high-frequency information. The low-frequency component represents the mean value and the high-frequency component represents the difference value. The mean value, classified as low-frequency information, captures gradual changes and encodes both the picture's contour information and approximate details. Conversely, the difference value, characterized as high-frequency information, captures rapid changes and encodes intricate picture details as well as local information (including noise). As a result, we utilize the DWT to extract and retain the LL subband images, which are employed in the preparation of Stage-2 and Stage-3. This decision effectively preserves contour information and reduces noise interference.

2) *Normalization*: Normalization entails constraining data within a desired range, with the goal of simplifying subsequent data processing and expediting convergence. The governing equation for this process is expressed as:

$$I_N = (IV_{n\max} - IV_{n\min}) \frac{1}{1 + e^{-\frac{I-\beta}{\alpha}}} + IV_{n\min} \quad (5)$$

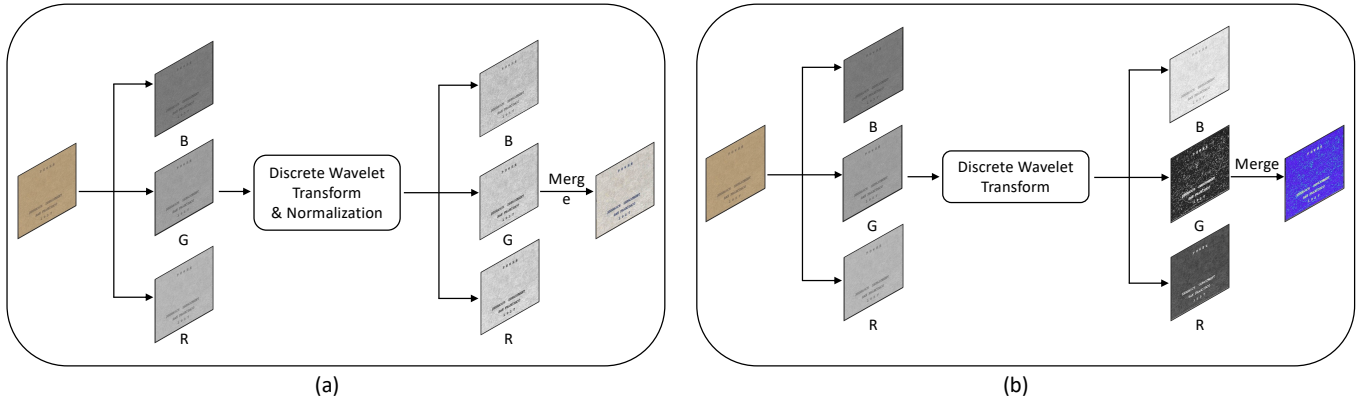


Fig. 3. Example of image normalization from HW15 of DIBCO 2011 dataset: (a) Normalization after DWT retains LL subband images, (b) No normalization after DWT retains LL subband images.

where IV is the intensity values, the image to be processed $I : \{\mathbb{X} \subseteq \mathbb{R}^n\} \rightarrow \{IV_{\min}, \dots, IV_{\max}\}$, and the generated image $I_N : \{\mathbb{X} \subseteq \mathbb{R}^n\} \rightarrow \{IV_{n\min}, \dots, IV_{n\max}\}$. α defines the width of the input intensity range, and β defines the range centered intensity.

In our method, we normalize the LL subband images to render initially incomparable data amenable to comparison, all the while preserving the relative relationships between the compared datasets. An illustrative example of the impact of normalization on RGB component images post DWT is provided in Fig. 3. For instance, when applied to the image HW15 from the DIBCO 2011 dataset, normalization effectively balances the RGB components. In contrast, failing to apply normalization results in an output image heavily skew towards the blue component. A comprehensive investigation into the influence of normalization on experimental outcomes is expounded upon in the comparative experiment outlined in Section IV-E.

C. Stage-2

In Stage-2, the method proposed in this work is illustrated in Fig. 4. Initially, the original input image is partitioned into four distinct channels. Each of these channels is processed by an independent generator. Furthermore, a shared discriminator is employed across all channels to differentiate between the generated images and their corresponding ground truth counterparts. The four generators are individually trained using images originating from the red, green, blue, and gray channels, respectively. As a result, the trained adversarial networks have the capability to eliminate background information from localized image blocks while simultaneously extracting the colored foreground details.

1) *Network architecture*: The generator employs an encoder-decoder architecture, utilizing the U-Net++ framework [37], [38]. Within the generator, encoders serve to extract features, while a shared encoder is employed alongside multiple decoders of varying depths, subsequently concatenated. The encoder facilitates downsampling and context extraction, while the decoders undertake upsampling and amalgamate both upsampled and downsampled features. The encoder em-

Algorithm 1 Training process for GAN using the output images of Stage-1

Require: Adam optimizer, $\eta = 1 \times 10^{-4}$

Ensure: $\omega = 0.5$, $\alpha = 10$, $\lambda = 50$

- 1: **Initialize:** Parameters $\theta_{G_r}, \theta_{G_g}, \theta_{G_b}, \theta_{G_{gray}}$
- 2: **for** number of training iterations **do**
- 3: Input Image Split into $r, g, b, gray$ images
- 4: **for** $k = \{r, g, b, gray\}$ **do**
- 5: **if** k is gray **then**
- 6: $y_k \leftarrow y$
- 7: **else**
- 8: $x'_k = Norm(V_{LL}(x_k))$
- 9: $y_k \leftarrow x'_k \cap y$
- 10: Binarize y_k with threshold value t .
- 11: **end if**
- 12: Update Discriminator D (Eq. (6)):
- 13: $\theta_D \leftarrow \theta_D - \eta_D \nabla_{\theta_D} \mathbb{L}_D$
- 14: Update Generator G_k (Eq. (7)):
- 15: $\theta_{G_k} \leftarrow \theta_{G_k} - \eta_G \nabla_{\theta_{G_k}} \mathbb{L}_G$
- 16: **end for**
- 17: **end for**
- 18: **for** $k = \{r, g, b\}$ **do**
- 19: $\hat{y}_k \leftarrow \omega G_k(x_k) + (1 - \omega) G_{gray}(x_{gray})$
- 20: **end for**
- 21: $\hat{y} \leftarrow [\hat{y}_r, \hat{y}_g, \hat{y}_b]$

plies EfficientNet [39], a lightweight CNN recognized for its strong performance in image classification tasks. To enhance generalization, the discriminator within the network architecture is upgraded following the principles of PatchGAN [40], [41], [42].

Given the unpredictability of color document degradation, this work adopts four distinct adversarial networks to extract text information from diverse colored backgrounds. This method mitigates color interference during document image binarization. Notably, the discriminator necessitates uniform channel input images, a consideration arising from the generator's production of four-channel (red, green, blue, and gray) images, whereas the ground truth image consists solely of

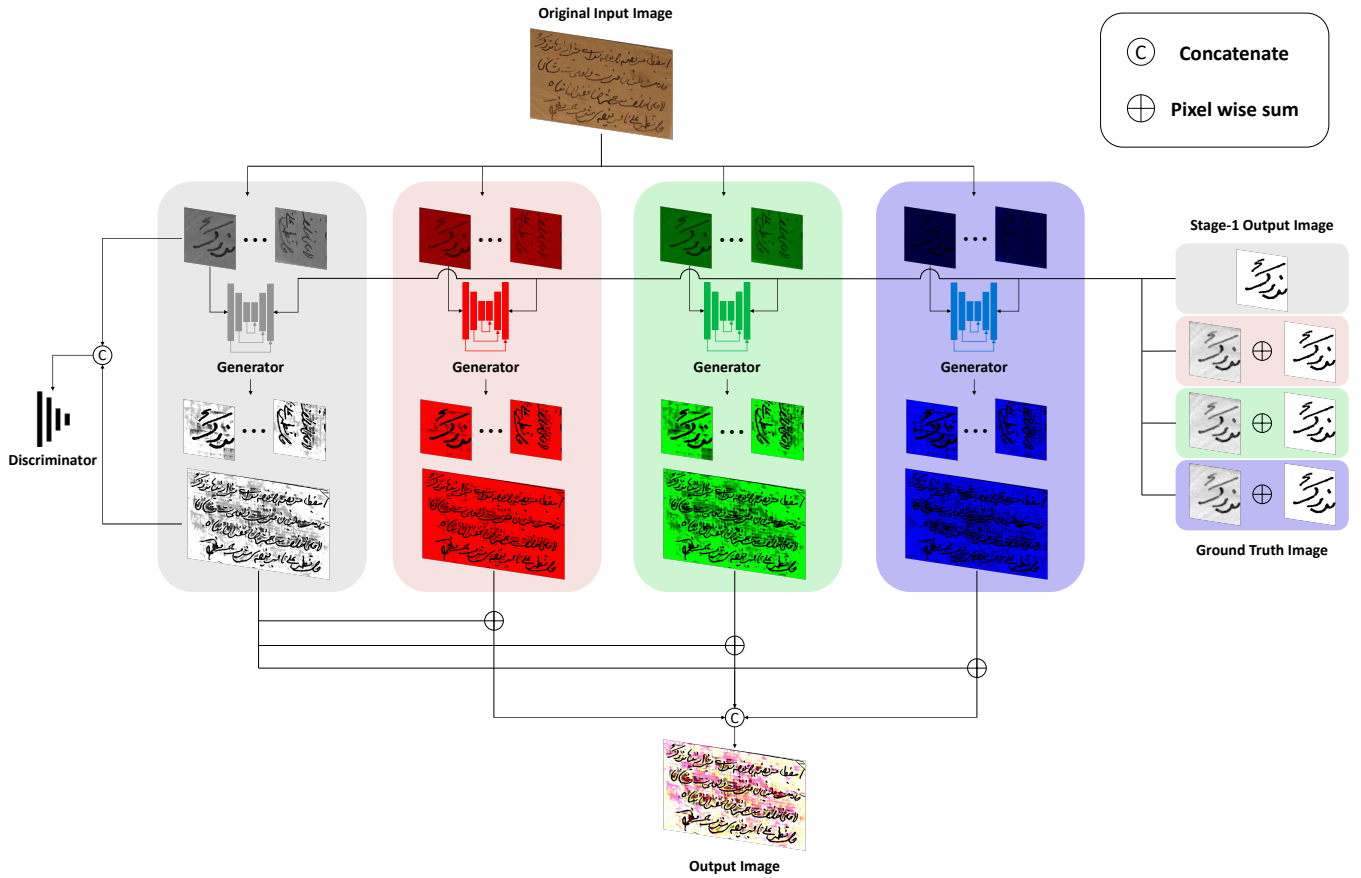


Fig. 4. The architecture diagram of the stage-2 of the proposed method. This method employs U-Net++ architecture with EfficientNet as the generator and PatchGAN as the discriminator. The ground truth image during the training process is derived through pixel-wise summation of the dataset-provided image and the output from stage-1.

one channel (grayscale). To align with this requirement, we merge the three single-channel output images (red, green, and blue) from Stage-1 with the ground truth image, ensuring compatibility with the input discriminator.

2) *Loss functions of GAN*: To ensure a more robust convergence of the loss function, we employ the Wasserstein Generative Adversarial Network with Gradient Penalty (WGAN-GP) [43] on the objective function. Empirical investigations conducted by Bartusiak *et al.* [44] have demonstrated that the binary cross-entropy (BCE) loss yields superior performance compared to the $L1$ loss in binary classification tasks. Therefore, we opt for the utilization of the BCE loss instead of the $L1$ loss used in the Pix2Pix GAN framework [29]. The loss function of the WGAN-GP target, which incorporates the BCE loss, is formulated as follows:

$$\mathbb{L}_D = -\mathbb{E}_{x,y}[D(y,x)] + \mathbb{E}_x[D(G(x),x)] + \alpha \mathbb{E}_{x,\hat{y} \sim P_{\hat{y}}}[(\|\nabla_{\hat{y}} D(\hat{y},x)\|_2 - 1)^2] \quad (6)$$

$$\mathbb{L}_G = \mathbb{E}_x[D(G(x),x)] + \lambda \mathbb{E}_{G(x),y}[y \log G(x) + (1-y) \log(1-G(x))] \quad (7)$$

where the penalty coefficient is α , and the uniform sampling along a straight line between the ground truth distribution P_y and the point pairs of the generated data distribution is $P_{\hat{y}}$. λ is used to control the relative importance of different loss

terms. The parameter of the generator is θ_G and the parameter of the discriminator is θ_D . In the discriminator, the generated image is distinguished from the real image by the target loss function \mathbb{L}_D in Eq. (6). In the generator, the distance between the generated image and the ground truth image in each color channel is minimized by the target loss function \mathbb{L}_G in Eq. (7).

The detailed procedure for training GAN models is illustrated in Algorithm 1. The training process is conducted within a specially designed environment, encompassing optimizer selection, learning rate configuration, and loss function definition. The algorithm demonstrates that the GAN model iteratively updates the loss function based on the authenticity assessment of the generated image by the discriminator. This iterative process enhances the ability of the generator to produce more realistic images.

D. Stage-3

In Stage-3, a multi-scale adversarial network is employed to generate images for both local and global binarization results, enhancing the distinction between the background and text parts with higher accuracy. Contrary to Stage-2, which predominantly relies on local predictions using small patches, Stage-3 conducts global binarization on the original input image size. This addresses the contextual information loss in

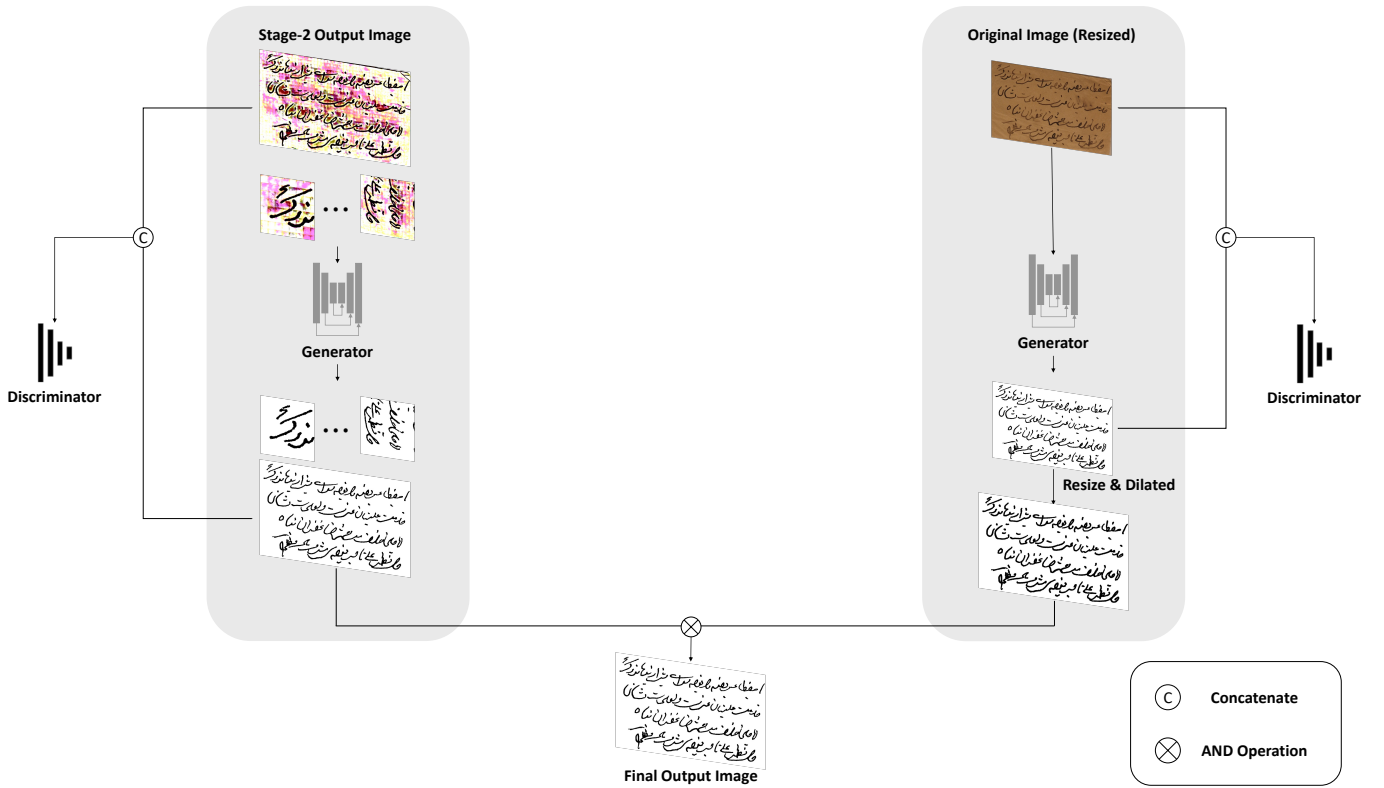


Fig. 5. The architecture diagram of the stage-3 of the proposed method. This stage comprises both local and global predictions. Local prediction involves training several 224×224 size patches, while global prediction involves directly resizing the original image to 448×448 for training.

text images caused by the local predictions in the second stage. Fig. 5 illustrates the usage of two discriminators in Stage-3, necessitated by Stage-2 utilization of 8-bit images for local prediction, while Stage-3 uses 24-bit, three-channel images. Additionally, the figure clarifies that the left-side input image comprises small patches from the Stage-2 output, intended for local prediction. Conversely, the right-side input image represents the original input image for global prediction. In Stage-3 of the binarization process, the generator's network architecture remains consistent with Stage-2, differing only in the number of input channels. In the case of public datasets like DIBCO, the provided document images encompass a range of scales. Hence, in Stage-3, we perform direct binarization of the original input images by resizing them to the required dimensions.

IV. EXPERIMENTS

A. Datasets

We compared the proposed method with several classic and SOTA methods on multiple public datasets. For the training set, we selected 10 images from DIBCO 2009 [58], 10 images from H-DIBCO 2010 [59], 15 images from the Persian Heritage Image Binarization Dataset (PHIBD) [60], 14 images from H-DIBCO 2012 [61], 87 images from the Synchronmedia Multispectral Ancient Document Images Dataset (SMADI) [1], and 7 images from the Bickley Diary Dataset [62]. In total, our training set has 143 images. Additionally, the test sets consist of 16 images from DIBCO 2011 [11], 16 images

from DIBCO 2013 [13], 10 images from H-DIBCO 2014 [12], 10 images from H-DIBCO 2016 [14], 20 images from DIBCO 2017 [16], and 10 images from H-DIBCO2018 [15]. In summary, a total of 82 images are used for testing.

1) *DIBCO*: The Document Image Binarization Competition (DIBCO) provides several datasets: DIBCO 2009, H-DIBCO 2010, DIBCO 2011, H-DIBCO 2012, DIBCO 2013, DIBCO 2017, H-DIBCO 2014, H-DIBCO 2016, and H-DIBCO 2018. These datasets comprise both grayscale and color images, including machine-printed as well as handwritten content. Participants in the competition were tasked with designing algorithms capable of extracting binarized text images from both handwritten and machine-printed images within these datasets.

2) *PHIBD*: The Persian Heritage Image Binarization Dataset (PHIBD) contains 15 images of historical manuscripts from Mirza Mohammad Kazemai's old manuscript library in Yazd, Iran. The images within the dataset have suffered from various types of degradation, including bleeding, fading, and blurring.

3) *SMADI*: The Synchronmedia Multispectral Ancient Document Images Dataset (SMADI) consists of 240 multispectral images of 30 authentic historical handwritten letters. These letters, dating from the 17th to the 20th centuries, were written using iron gall ink. The original documents are deposited at the BANQ Bibliotheque et Archives nationales du Quebec. A total of 240 images of real documents were meticulously captured, calibrated, and registered within this dataset. Each of these images was imaged with a CROMA CX MSI camera, resulting



Fig. 6. Example of images enhancement and binarization in the DIBCO dataset: (a) the original input image, (b) the LL subband image obtained by applying discrete wavelet transform and normalization (Stage-1), (c) the enhanced image produced using our image enhancement method (Stage-2), (d) the binarized image obtained by combining local and global predictions (Stage-3), (e) the ground truth image.

in 8 images per document.

4) *Bickley Diary Dataset*: The Bickley Diary Dataset has been generously donated to the Singapore Methodist Archives by Erin Bickley. This dataset comprises diaries in which the images have been affected by both light and fold damage, thereby complicating the process of identification.

B. Evaluation Metric

In comparison with other classic and SOTA methods for document image binarization, we use the following four evaluation metrics:

1) F-measure (FM):

$$FM = \frac{2 \times Recall \times Precision}{Recall + Precision} \quad (8)$$

where Recall is defined as $\frac{TP}{TP+FN}$, Precision is defined as $\frac{TP}{TP+FP}$, and TP, FP, and FN represent the true positive, false positive, and false negative values, respectively.

2) Pseudo-F-measure (p-FM):

$$p-FM = \frac{2 \times Recall_{ps} \times Precision_{ps}}{Recall_{ps} + Precision_{ps}} \quad (9)$$

where Pseudo-Recall ($Recall_{ps}$) and Pseudo-Precision ($Precision_{ps}$) both use the distance weights relative to the ground truth image profile to generate a new weighted ground truth image.

3) Peak signal-to-noise ratio (PSNR):

$$PSNR = 10 \log\left(\frac{V^2}{MSE}\right) \quad (10)$$

where MSE (Mean Square Error) is defined as:

$$MSE = \frac{\sum_{x=1}^{width} \sum_{y=1}^{height} (L(x, y) - L'(x, y))^2}{width \times height} \quad (11)$$

where V represents the difference between the foreground and background. Generally, a higher PSNR indicates

TABLE I

COMPARISON EXPERIMENT OF INPUT IMAGE AND GROUND TRUTH (GT) IMAGE USING DISCRETE WAVELET TRANSFORM (DWT) AND NORMALIZATION

(a) DIBCO 2011						(b) DIBCO 2013					
Input	GT	FM \uparrow	p-FM \uparrow	PSNR \uparrow	DRD \downarrow	Input	GT	FM \uparrow	p-FM \uparrow	PSNR \uparrow	DRD \downarrow
Original	Original	86.68	89.61	19.27	4.01	Original	Original	92.94	94.70	21.57	2.74
Original	DWT	88.20	90.57	19.53	3.45	Original	DWT	94.43	95.64	21.79	2.13
Original	DWT+Norm	87.70	90.24	19.65	3.45	Original	DWT+Norm	94.88	96.19	22.32	1.95
DWT	Original	87.74	89.69	18.88	3.78	DWT	Original	93.23	94.43	20.80	2.67
DWT+Norm	Original	89.33	91.94	19.49	3.37	DWT+Norm	Original	93.76	95.41	21.54	2.40
DWT	DWT	90.53	92.82	19.68	3.11	DWT	DWT	94.39	95.34	21.91	2.26
DWT+Norm	DWT+Norm	89.06	92.25	19.59	3.31	DWT+Norm	DWT+Norm	94.55	95.86	22.02	2.07

(c) H-DIBCO 2014						(d) H-DIBCO 2016					
Input	GT	FM \uparrow	p-FM \uparrow	PSNR \uparrow	DRD \downarrow	Input	GT	FM \uparrow	p-FM \uparrow	PSNR \uparrow	DRD \downarrow
Original	Original	96.50	97.50	22.08	1.01	Original	Original	90.74	94.46	19.39	3.30
Original	DWT	96.52	97.70	22.15	0.99	Original	DWT	91.76	95.74	19.67	2.93
Original	DWT+Norm	96.88	98.03	22.68	0.89	Original	DWT+Norm	91.49	96.46	19.68	2.92
DWT	Original	95.94	96.91	21.31	1.19	DWT	Original	91.86	94.95	19.62	2.99
DWT+Norm	Original	96.29	97.48	22.05	1.16	DWT+Norm	Original	91.28	96.03	19.47	3.04
DWT	DWT	96.60	97.60	22.27	0.97	DWT	DWT	91.68	95.90	19.68	2.93
DWT+Norm	DWT+Norm	96.77	97.89	22.52	0.91	DWT+Norm	DWT+Norm	91.95	95.87	19.75	2.84

TABLE II

PERFORMANCE EVALUATION OF DIFFERENT METHODS FOR DOCUMENT BINARIZATION ON DIBCO 2011

AVG = (FM + p-FM + PSNR + (100-DRD)) / 4. BEST AND 2ND BEST PERFORMANCE ARE IN RED AND BLUE COLORS, RESPECTIVELY.

Method	Model	FM \uparrow	p-FM \uparrow	PSNR \uparrow	DRD \downarrow	Avg \uparrow
Niblack [18]	Thresholding	70.44	73.03	12.39	24.95	57.73
Otsu [17]	Thresholding	82.10	85.96	15.72	8.95	68.71
Sauvola et al. [19]	Thresholding	82.35	88.63	15.75	7.86	69.72
Vo et al. [45]	Thresholding	88.20	90.30	20.10	2.00	74.15
Howe [46]	Thresholding	92.28	90.79	19.01	4.46	74.41
Jia et al. [47]	Thresholding	95.56	91.65	18.88	2.66	75.86
Vo et al. [24]	CNN	92.58	94.67	19.16	2.38	76.01
He et al. [25]	CNN	91.92	95.82	19.49	2.37	76.22
Yang et al. [48]	CNN	93.44	95.82	20.10	2.25	76.78
Bhunia et al. [31]	CNN	93.70	96.80	20.10	1.80	77.20
Tensmeyer et al. [8]	CNN	93.60	97.70	20.11	1.85	77.39
Souibgui et al. [36]	Transformer	94.37	96.15	20.81	1.63	77.43
Zhao et al. [32]	GAN	92.62	95.38	19.58	2.55	76.26
Suh et al. [28]	GAN	93.44	96.18	19.97	1.93	76.92
Suh et al. [34]	GAN	93.57	95.93	20.22	1.99	76.93
Ours	GAN	94.08	97.08	20.51	1.75	77.48

greater similarity between the images.

- 4) Distance reciprocal distortion (DRD):

$$DRD = \frac{\sum_k DRD_k}{NUBN} \quad (12)$$

where DRD_k is defined as:

$$DRD_k = \sum_{i=-2}^2 \sum_{j=-2}^2 |G_k(i,j) - B_k(x,y)| \times N_w(i,j) \quad (13)$$

where DRD represents a measure of visual distortion in the binary image. NUBN corresponds to the number of uneven 8×8 blocks in the ground truth image, while DRD_k indicates the distortion of the k_{th} flipped pixel, calculated using a 5×5 normalized weight matrix N_w . B_k refers to the pixel of the binary image, and G_k denotes the pixel of the ground truth image.

C. Implementation Details

The experiments were conducted using the PyTorch framework in Python, employing the NVIDIA RTX 3090 GPU for the training process.

1) *Data preparation*: To ensure a fair comparison of performance among all methods, we used the same data augmentation and training sets for our method and other SOTA methods. During the training process of the local prediction network, we cut the input images into 224×224 patches. These patches were sampled with scale factors of 0.75, 1.25, 1.5, subsequently resized to 224×224 , and rotated by 270° . This data augmentation process generated a total of 336,702 training image patches from the dataset. In contrast, for training the global prediction network, this work employed scaling without rotation for data augmentation, using a scaling size of 448×448 . To diversify the training data, rotation augmentation was applied to the global prediction, involving rotations of 90° , 180° , and 270° , as well as horizontal and vertical flips. This data augmentation process resulted in a set

TABLE III

PERFORMANCE EVALUATION OF DIFFERENT METHODS FOR DOCUMENT BINARIZATION ON DIBCO 2013
 AVG = (FM + p-FM + PSNR + (100-DRD)) / 4. BEST AND 2ND BEST PERFORMANCE ARE IN RED AND BLUE COLORS, RESPECTIVELY.

Method	Model	FM \uparrow	p-FM \uparrow	PSNR \uparrow	DRD \downarrow	Avg \uparrow
Niblack [18]	Thresholding	71.38	73.17	13.54	23.10	58.75
Otsu [17]	Thresholding	80.04	83.43	16.63	10.98	67.28
Sauvola et al. [19]	Thresholding	82.73	88.37	16.98	7.34	70.19
Howe [46]	Thresholding	91.30	91.70	21.30	3.20	75.28
Xiong et al. [49]	Thresholding	93.50	94.40	21.30	2.70	76.63
Vo et al. [24]	Thresholding	93.43	95.34	20.82	2.26	76.83
Jia et al. [47]	Thresholding	93.28	96.58	20.76	2.01	77.15
Tensmeyer et al. [8]	CNN	93.10	96.80	20.70	2.20	77.10
He et al. [25]	CNN	93.36	96.70	20.88	2.15	77.20
Yang et al. [48]	CNN	95.19	96.37	22.58	1.78	78.09
Zhao et al. [32]	GAN	93.86	96.47	21.53	2.32	77.39
Suh et al. [34]	GAN	95.01	96.49	21.99	1.76	77.93
Suh et al. [28]	GAN	94.75	97.36	21.78	1.73	78.04
Ours	GAN	95.24	97.51	22.27	1.59	78.36

TABLE IV

PERFORMANCE EVALUATION OF DIFFERENT METHODS FOR DOCUMENT BINARIZATION ON H-DIBCO 2014
 AVG = (FM + p-FM + PSNR + (100-DRD)) / 4. BEST AND 2ND BEST PERFORMANCE ARE IN RED AND BLUE COLORS, RESPECTIVELY.

Method	Model	FM \uparrow	p-FM \uparrow	PSNR \uparrow	DRD \downarrow	Avg \uparrow
Niblack [18]	Thresholding	86.01	88.04	16.54	8.26	70.58
Sauvola et al. [19]	Thresholding	83.72	87.49	17.48	5.05	70.91
Otsu [17]	Thresholding	91.62	95.69	18.72	2.65	75.85
Jia et al. [47]	Thresholding	94.89	97.68	20.53	1.50	77.90
Howe [46]	Thresholding	96.49	97.38	22.24	1.08	78.76
Vo et al. [24]	CNN	95.97	97.42	21.49	1.09	78.45
He et al. [25]	CNN	95.95	98.76	21.60	1.12	78.80
Yang et al. [48]	CNN	96.66	97.26	23.13	1.21	78.96
Suh et al. [28]	GAN	96.19	97.13	21.77	1.14	78.49
Zhao et al. [32]	GAN	96.09	98.25	21.88	1.20	78.76
Suh et al. [34]	GAN	96.36	97.87	21.96	1.07	78.78
Ours	GAN	96.65	98.19	22.27	0.96	79.04

of 1,890 training image patches.

2) *Training*: The training parameters for the Stage-2 and Stage-3 were consistent, differing solely in the number of training epochs: 150 epochs for global prediction and 10 epochs for the remaining networks. The choice of optimizer was Adam [63], with a learning rate set at 2×10^{-4} . Additionally the generator employed $\beta_1 = 0.5$, while the discriminator used $\beta_2 = 0.999$.

3) *Pre-training*: To enhance training efficacy due to limited data availability, we employed EfficientNet [39] as the encoder in the generator, utilizing weights pretrained on the ImageNet dataset [64].

D. Comparison with other Methods

Our proposed method was evaluated in the DIBCO datasets, and four evaluation metrics are presented in Section IV-B to compare different methods, including the traditional binarization methods employing Thresholding and SOTA methods based on CNN, Transformer and GAN. It is important to note that not all methods were tested on these six DIBCO datasets, leading to variations in the methods compared on each dataset.

E. Comparison Experiment

In Stage-1, we apply DWT and normalization to 224×224 split images. Although the mathematical theory demonstrates

that the processed images can effectively retain contour information and minimize noise, we aim to comprehensively assess the influence of these processed images on the experimental outcomes.

In this section, a comparison experiment is conducted to find out that whether the output images from Stage-1 would have better performance when utilized as Stage-2 input images and the corresponding ground truth images. This work utilizes UNet++ [38] architecture with EfficientNet [39] as the generator to evaluate the network model on the datasets DIBCO 2011, DIBCO 2013, H-DIBCO 2014, and H-DIBCO 2016. For the input images of the generator, three distinct configurations are established: (1) original input image, (2) LL subband image retained by DWT, and (3) LL subband image retained by DWT followed by normalization. For the corresponding ground truth images of the generator, except for the ground truth channel (1-D), it sets three configurations for the images of the other three channels, which are used in the same way as the input images.

Table I presents a comparative analysis of various configurations along with their corresponding model performances across four datasets. On these four datasets, the configuration that directly employs the original image as input and corresponding ground truth image provides the worst performance. Table I (a) indicates that the configuration using only DWT without normalization as input and corresponding ground truth

TABLE V

PERFORMANCE EVALUATION OF DIFFERENT METHODS FOR DOCUMENT BINARIZATION ON H-DIBCO 2016
 AVG = (FM + p-FM + PSNR + (100-DRD)) / 4. BEST AND 2ND BEST PERFORMANCE ARE IN RED AND BLUE COLORS, RESPECTIVELY.

Method	Model	FM \uparrow	p-FM \uparrow	PSNR \uparrow	DRD \downarrow	Avg \uparrow
Niblack [18]	Thresholding	72.57	73.51	13.26	24.65	58.67
Sauvola et al. [19]	Thresholding	84.27	89.10	17.15	6.09	71.11
Otsu [17]	Thresholding	86.59	89.92	17.79	5.58	72.18
Vo et al. [45]	Thresholding	87.30	90.50	17.50	4.40	72.73
Howe [46]	Thresholding	87.47	92.28	18.05	5.35	73.11
Bera et al. [50]	Thresholding	90.43	91.66	18.94	3.51	74.38
Jia et al. [47]	Thresholding	90.10	93.72	19.00	4.03	74.70
Vo et al. [24]	CNN	90.01	93.44	18.74	3.91	74.57
Yang et al. [48]	CNN	90.41	94.70	19.00	3.34	75.19
He et al. [25]	CNN	91.19	95.74	19.51	3.02	75.86
Kang et al. [51]	CNN	93.09	94.85	19.18	3.03	76.02
Bhunja et al. [31]	CNN	92.30	95.40	19.90	2.70	76.23
Westphal et al. [52]	RNN	88.80	92.50	18.40	3.90	73.95
Guo et al. [53]	Diffusion	88.51	90.46	18.42	4.13	73.32
Zhao et al. [32]	GAN	89.77	94.58	18.80	3.85	74.83
Suh et al. [28]	GAN	91.11	95.22	19.34	3.25	75.61
Suh et al. [34]	GAN	92.24	95.95	19.93	2.77	76.34
Ours	GAN	91.46	96.32	19.66	2.94	76.13

TABLE VI

PERFORMANCE EVALUATION OF DIFFERENT METHODS FOR DOCUMENT BINARIZATION ON DIBCO 2017
 AVG = (FM + p-FM + PSNR + (100-DRD)) / 4. BEST AND 2ND BEST PERFORMANCE ARE IN RED AND BLUE COLORS, RESPECTIVELY.

Method	Model	FM \uparrow	p-FM \uparrow	PSNR \uparrow	DRD \downarrow	Avg \uparrow
Otsu [17]	Thresholding	77.73	77.89	13.85	15.54	63.48
Sauvola et al. [19]	Thresholding	77.11	84.10	14.25	8.85	66.65
Bera et al. [50]	Thresholding	83.38	89.43	15.45	6.71	70.39
Jia et al. [47]	Thresholding	85.66	88.30	16.40	7.67	70.67
Howe [46]	Thresholding	90.10	90.95	18.52	5.12	73.61
Kang et al. [51]	CNN	91.57	93.55	15.85	2.92	74.51
Yang et al. [48]	CNN	91.33	93.84	18.34	3.24	75.07
Jemni et al. [54]	GAN	89.80	89.95	17.45	4.03	73.29
Zhao et al. [32]	GAN	90.73	92.58	17.83	3.58	74.39
Suh et al. [28]	GAN	90.95	94.65	18.40	2.93	75.27
Ours	GAN	90.95	93.79	18.57	2.94	75.09

image performs well on DIBCO 2011 dataset. Tables I (b) and (c) demonstrate that the configuration that inputs the original images directly, and employs Stage-1 output images as the corresponding ground truth images provides the best performance on DIBCO 2013 and H-DIBCO 2014 datasets. In addition, the above configuration in Table I (d) achieves the highest p-FM value. Therefore, we choose this configuration to construct our network model architecture.

F. Ablation Study

In the comparison experiments detailed in Section IV-E, it demonstrates that training the generator following DWT and image normalization significantly enhances the performance of the network model. However, we would like to show the advantages of each stage better, and we have selected 5 images from PHIBD and Bickley Diary Dataset. These images are employed to systematically exhibit the results of image enhancement and binarization through the step-by-step application of different stages of our proposed method. As shown in Fig. 6, (b) represents the result of retaining the LL subband images after applying DWT and normalization. This stage performs noise reduction on the original input image, which is used as the ground truth image for the generator.

Fig. 6 (c) showcases the result of image enhancement achieved using adversarial networks, where the image has had the background color removed and the color of the text highlighted. Fig. 6 (d) is the final output image obtained using the proposed whole method. Notably, it is evident that our final output result closely approximate the ground truth image, as evident from Figure 6 (e).

G. Experimental Results

In this work, different models are evaluated on six DIBCO datasets (DIBCO 2011, DIBCO 2013, H-DIBCO 2014, H-DIBCO 2016, DIBCO 2017, and H-DIBCO 2018). Since the DIBCO datasets do not provide OCR output, this work uses the four evaluation metrics introduced in Section IV-B to evaluate the proposed method and SOTA method.

The results of the model evaluation on the six DIBCO datasets are presented in Tables II, III, IV, V, VI, and VII. The tables illustrate that the proposed method consistently ranks among the top three performers across all metrics. However, due to variations in the rankings based on the four distinct evaluation metrics, a clear representation of the model performance becomes challenging. To address this, we introduce the average metric (Avg). The specific formula for

TABLE VII

PERFORMANCE EVALUATION OF DIFFERENT METHODS FOR DOCUMENT BINARIZATION ON H-DIBCO 2018
 AVG = (FM + p-FM + PSNR + (100-DRD)) / 4. BEST AND 2ND BEST PERFORMANCE ARE IN RED AND BLUE COLORS, RESPECTIVELY.

Method	Model	FM \uparrow	p-FM \uparrow	PSNR \uparrow	DRD \downarrow	Avg \uparrow
Otsu [17]	Thresholding	51.45	53.05	9.74	59.07	38.79
Sauvola et al. [19]	Thresholding	67.81	74.08	13.78	17.69	59.50
Jia et al. [47]	Thresholding	76.05	80.36	16.90	8.13	66.30
Bera et al. [50]	Thresholding	76.84	83.58	15.31	9.58	66.54
Howe [46]	Thresholding	80.84	82.85	16.67	11.96	67.10
Akbari et al. [55]	CNN	89.05	93.65	19.17	4.80	74.27
Kang et al. [51]	CNN	89.71	91.62	19.39	2.51	74.55
Yang et al. [48]	CNN	91.09	94.57	19.92	3.07	75.63
Souibgui et al. [36]	Transformer	90.59	93.97	19.46	3.35	75.17
Souibgui et al. [56]	GAN	77.59	85.74	16.16	7.93	67.89
Tamrin et al. [57]	GAN	83.08	88.46	17.04	5.09	70.87
Zhao et al. [32]	GAN	87.73	90.60	18.37	4.58	73.03
Jemni et al. [54]	GAN	92.41	94.35	20.18	2.60	76.09
Suh et al. [28]	GAN	91.86	96.25	20.03	2.60	76.39
Ours	GAN	91.66	95.53	20.02	2.81	76.10

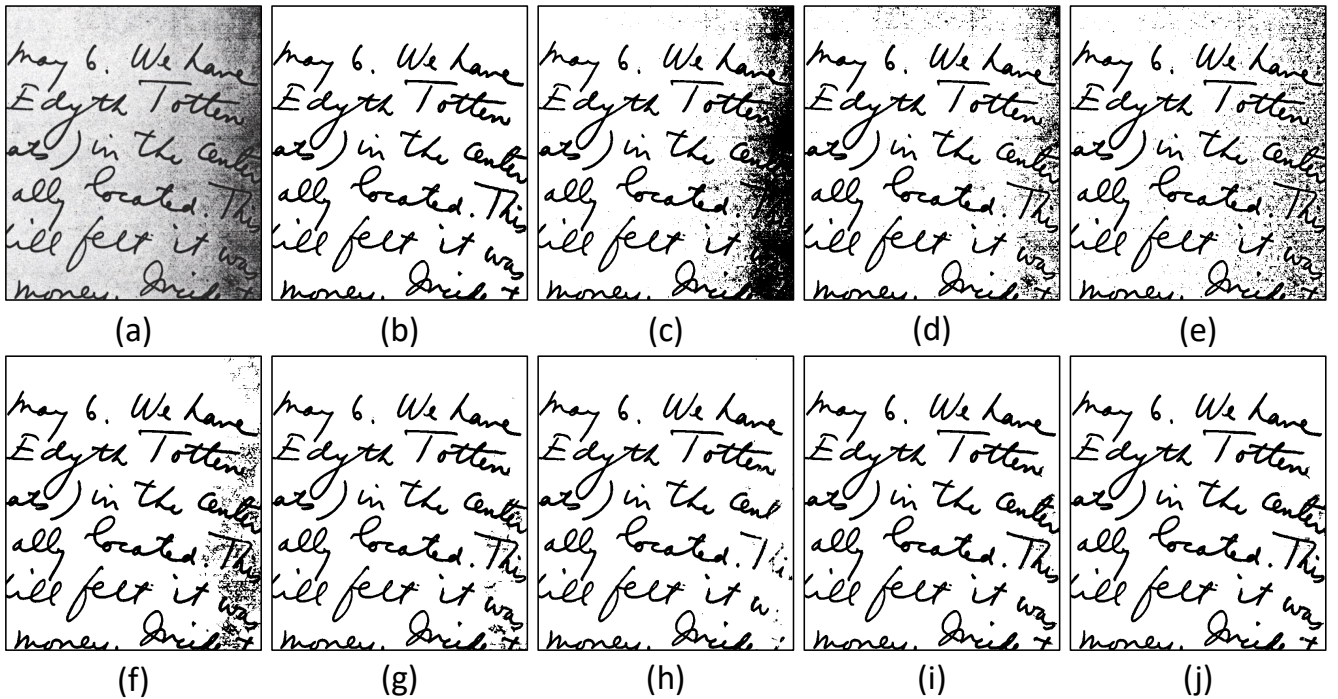


Fig. 7. Example of document image binarization results from the input image HW1 of DIBCO 2011 dataset by different methods: (a) original input images, (b) the ground truth, (c) Otsu [17], (d) Niblack [18], (e) Sauvola [19], (f) Vo [24], (g) He [25], (h) Zhao [32], (i) Suh [28], (j) Ours.

this metric is as follows:

$$Avg = (FM + p - FM + PSNR + (100 - DRD)) / 4 \quad (14)$$

On the DIBCO 2011, DIBCO 2013, and H-DIBCO 2014 datasets, the proposed model achieves the highest average (Avg) value, surpassing other state-of-the-art models. In the case of the H-DIBCO 2016, DIBCO 2017, and H-DIBCO 2018 datasets, our model achieves the second-highest Avg values: 76.13, 75.09, and 76.10, respectively. These values are slightly lower than the highest recorded values, namely 76.34, 75.27, and 76.39. These results show that the proposed method is more effective than the SOTA method for binarization of degraded color documents.

In addition to assessing method performance by comparing quantitative metrics across various approaches, this study aims to provide readers with an intuitive understanding of the distinctions through application results involving images. Consequently, we have chosen images from the DIBCO 2011 and DIBCO 2013 datasets to illustrate examples of binarization outcomes. Figs. 7, 8, and 9 depict the binarization results for images HW1, HW5, and PR16, utilizing diverse methodologies. The figures demonstrate that the SOTA method outperforms the traditional binarization approach in terms of shadow and noise elimination. Furthermore, the proposed method excels in preserving textual content while effectively mitigating the presence of shadows and noise.

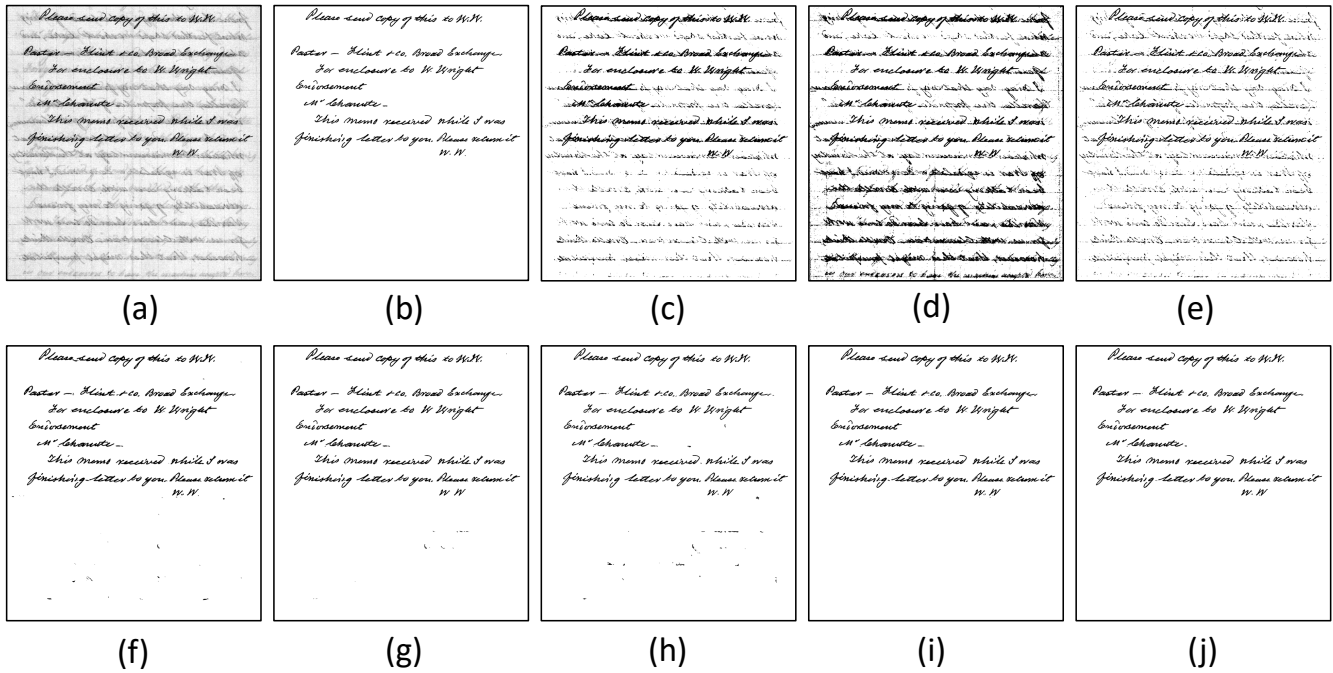


Fig. 8. Example of document image binarization results from the input image HW5 of DIBCO 2013 dataset by different methods: (a) original input images, (b) the ground truth, (c) Otsu [17], (d) Niblack [18], (e) Sauvola [19], (f) Vo [24], (g) He [25], (h) Zhao [32], (i) Suh [28], (j) Ours.

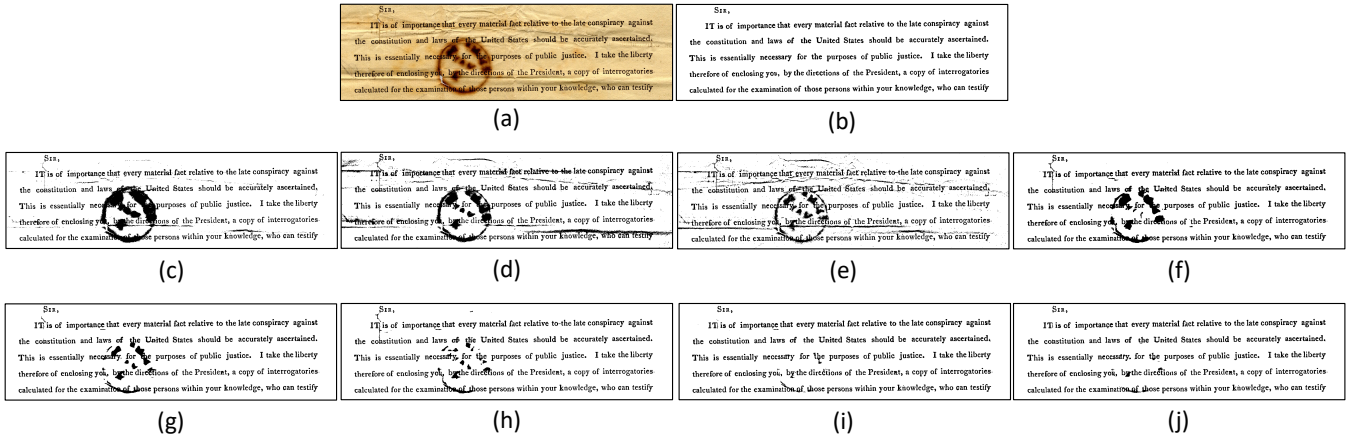


Fig. 9. Example of document image binarization results from the input image PR16 of DIBCO 2013 dataset by different methods: (a) original input images, (b) the ground truth, (c) Otsu [17], (d) Niblack [18], (e) Sauvola [19], (f) Vo [24], (g) He [25], (h) Zhao [32], (i) Suh [28], (j) Ours.

V. CONCLUSION

This paper introduces a novel three-stage method based on generative adversarial networks to address the issue of text degradation in degraded document images with color backgrounds, utilizing the DWT. The proposed method involves preserving the LL subband images through DWT to eliminate image noise, serving as ground truth for the generator. It trains independent networks utilizing single-channel images from four different colors, followed by a fusion of local and global prediction networks for binarization. As far as our knowledge extends, this work represents the first three-stage method that combines traditional image processing with deep learning. The experimental results demonstrate that employing U-Net++ as the generator and PatchGAN as the discriminator outperforms

performance compared to other SOTA methods.

The proposed three-stage architecture serves as a versatile foundational framework capable of accommodating diverse neural network training. The utilization of advanced networks in roles such as segmentation architecture and generator encoders can notably enhance the performance of this framework. It is worth noting that self-attention mechanisms have recently stood out in computer vision tasks. In the future work, we plan to apply self-attention mechanisms to generators, aiming to attain more efficient network models and further the progress of document image binarization.

REFERENCES

- [1] R. Hedjam and M. Cheriet, "Historical document image restoration using multispectral imaging system," *Pattern Recognition*, vol. 46, no. 8, pp. 2297–2312, 2013.
- [2] B. Sun, S. Li, X.-P. Zhang, and J. Sun, "Blind bleed-through removal for scanned historical document image with conditional random fields," *IEEE Transactions on Image Processing*, vol. 25, no. 12, pp. 5702–5712, 2016.
- [3] N. Kligler, S. Katz, and A. Tal, "Document enhancement using visibility detection," in *Proceedings of the IEEE Conference on Computer Vision and Pattern Recognition*, 2018, pp. 2374–2382.
- [4] A. Sulaiman, K. Omar, and M. F. Nasrudin, "Degraded historical document binarization: A review on issues, challenges, techniques, and future directions," *Journal of Imaging*, vol. 5, no. 4, p. 48, 2019.
- [5] J. Calvo-Zaragoza and A.-J. Gallego, "A selectional auto-encoder approach for document image binarization," *Pattern Recognition*, vol. 86, pp. 37–47, 2019.
- [6] X. Peng, H. Cao, K. Subramanian, R. Prasad, and P. Natarajan, "Exploiting stroke orientation for crf based binarization of historical documents," in *2013 12th International Conference on Document Analysis and Recognition*. IEEE, 2013, pp. 1034–1038.
- [7] J. Long, E. Shelhamer, and T. Darrell, "Fully convolutional networks for semantic segmentation," in *Proceedings of the IEEE conference on computer vision and pattern recognition*, 2015, pp. 3431–3440.
- [8] C. Tensmeyer and T. Martinez, "Document image binarization with fully convolutional neural networks," in *2017 14th IAPR international conference on document analysis and recognition (ICDAR)*, vol. 1. IEEE, 2017, pp. 99–104.
- [9] C.-H. Hsia, T.-Y. Lin, and J.-S. Chiang, "An adaptive binarization method for cost-efficient document image system in wavelet domain," *Journal of Imaging Science and Technology*, vol. 64, no. 3, pp. 30401–1, 2020.
- [10] R.-Y. Ju, Y.-S. Lin, J.-S. Chiang, C.-C. Chen, W.-H. Chen, and C.-T. Chien, "Ccdwt-gan: Generative adversarial networks based on color channel using discrete wavelet transform for document image binarization," *arXiv preprint arXiv:2305.17420*, 2023.
- [11] I. Pratikakis, B. Gatos, and K. Ntirogiannis, "Icdar 2011 document image binarization contest (dibco 2011)," in *2011 International Conference on Document Analysis and Recognition*. IEEE, 2011, pp. 1506–1510.
- [12] K. Ntirogiannis, B. Gatos, and I. Pratikakis, "Icfhr2014 competition on handwritten document image binarization (h-dibco 2014)," in *2014 14th International conference on frontiers in handwriting recognition*. IEEE, 2014, pp. 809–813.
- [13] I. Pratikakis, B. Gatos, and K. Ntirogiannis, "Icdar 2013 document image binarization contest (dibco 2013)," in *2013 12th International Conference on Document Analysis and Recognition*, 2013, pp. 1471–1476.
- [14] I. Pratikakis, K. Zagoris, G. Barlas, and B. Gatos, "Icfhr2016 handwritten document image binarization contest (h-dibco 2016)," in *2016 15th International Conference on Frontiers in Handwriting Recognition (ICFHR)*. IEEE, 2016, pp. 619–623.
- [15] I. Pratikakis, K. Zagori, P. Kaddas, and B. Gatos, "Icfhr 2018 competition on handwritten document image binarization (h-dibco 2018)," in *2018 16th International Conference on Frontiers in Handwriting Recognition (ICFHR)*. IEEE, 2018, pp. 489–493.
- [16] I. Pratikakis, K. Zagoris, G. Barlas, and B. Gatos, "Icdar2017 competition on document image binarization (dibco 2017)," in *2017 14th IAPR International Conference on Document Analysis and Recognition (ICDAR)*, vol. 1. IEEE, 2017, pp. 1395–1403.
- [17] N. Otsu, "A threshold selection method from gray-level histograms," *IEEE transactions on systems, man, and cybernetics*, vol. 9, no. 1, pp. 62–66, 1979.
- [18] W. Niblack, *An introduction to digital image processing*. Strandberg Publishing Company, 1985.
- [19] J. Sauvola and M. Pietikäinen, "Adaptive document image binarization," *Pattern recognition*, vol. 33, no. 2, pp. 225–236, 2000.
- [20] A. Krizhevsky, I. Sutskever, and G. E. Hinton, "Imagenet classification with deep convolutional neural networks," *Communications of the ACM*, vol. 60, no. 6, pp. 84–90, 2017.
- [21] M. D. Zeiler and R. Fergus, "Visualizing and understanding convolutional networks," in *European conference on computer vision*. Springer, 2014, pp. 818–833.
- [22] O. Ronneberger, P. Fischer, and T. Brox, "U-net: Convolutional networks for biomedical image segmentation," in *International Conference on Medical image computing and computer-assisted intervention*. Springer, 2015, pp. 234–241.
- [23] X. Peng, H. Cao, and P. Natarajan, "Using convolutional encoder-decoder for document image binarization," in *2017 14th IAPR international conference on document analysis and recognition (ICDAR)*, vol. 1. IEEE, 2017, pp. 708–713.
- [24] Q. N. Vo, S. H. Kim, H. J. Yang, and G. Lee, "Binarization of degraded document images based on hierarchical deep supervised network," *Pattern Recognition*, vol. 74, pp. 568–586, 2018.
- [25] S. He and L. Schomaker, "Deepotsu: Document enhancement and binarization using iterative deep learning," *Pattern recognition*, vol. 91, pp. 379–390, 2019.
- [26] I. Goodfellow, J. Pouget-Abadie, M. Mirza, B. Xu, D. Warde-Farley, S. Ozair, A. Courville, and Y. Bengio, "Generative adversarial networks," *Communications of the ACM*, vol. 63, no. 11, pp. 139–144, 2020.
- [27] A. Konwer, A. K. Bhunia, A. Bhowmick, A. K. Bhunia, P. Banerjee, P. P. Roy, and U. Pal, "Staff line removal using generative adversarial networks," in *2018 24th International Conference on Pattern Recognition (ICPR)*. IEEE, 2018, pp. 1103–1108.
- [28] S. Suh, H. Lee, P. Lukowicz, and Y. O. Lee, "Cegan: Classification enhancement generative adversarial networks for unraveling data imbalance problems," *Neural Networks*, vol. 133, pp. 69–86, 2021.
- [29] P. Isola, J.-Y. Zhu, T. Zhou, and A. A. Efros, "Image-to-image translation with conditional adversarial networks," in *Proceedings of the IEEE conference on computer vision and pattern recognition*, 2017, pp. 1125–1134.
- [30] M. Mirza and S. Osindero, "Conditional generative adversarial nets," *arXiv preprint arXiv:1411.1784*, 2014.
- [31] A. K. Bhunia, A. K. Bhunia, A. Sain, and P. P. Roy, "Improving document binarization via adversarial noise-texture augmentation," in *2019 IEEE International Conference on Image Processing (ICIP)*. IEEE, 2019, pp. 2721–2725.
- [32] J. Zhao, C. Shi, F. Jia, Y. Wang, and B. Xiao, "Document image binarization with cascaded generators of conditional generative adversarial networks," *Pattern Recognition*, vol. 96, p. 106968, 2019.
- [33] R. De, A. Chakraborty, and R. Sarkar, "Document image binarization using dual discriminator generative adversarial networks," *IEEE Signal Processing Letters*, vol. 27, pp. 1090–1094, 2020.
- [34] S. Suh, J. Kim, P. Lukowicz, and Y. O. Lee, "Two-stage generative adversarial networks for binarization of color document images," *Pattern Recognition*, vol. 130, p. 108810, 2022.
- [35] A. Nicolaou, V. Christlein, E. Riba, J. Shi, G. Vogeler, and M. Seuret, "Tormentor: Deterministic dynamic-path, data augmentations with fractals," in *Proceedings of the IEEE/CVF Conference on Computer Vision and Pattern Recognition*, 2022, pp. 2707–2711.
- [36] M. A. Souibgui, S. Biswas, S. K. Jemni, Y. Kessentini, A. Fornés, J. Lladós, and U. Pal, "Docentr: An end-to-end document image enhancement transformer," *arXiv preprint arXiv:2201.10252*, 2022.
- [37] Z. Zhou, M. M. Rahman Siddiquee, N. Tajbakhsh, and J. Liang, "Unet++: A nested u-net architecture for medical image segmentation," in *Deep learning in medical image analysis and multimodal learning for clinical decision support*. Springer, 2018, pp. 3–11.
- [38] Z. Zhou, M. M. R. Siddiquee, N. Tajbakhsh, and J. Liang, "Unet++: Redesigning skip connections to exploit multiscale features in image segmentation," *IEEE transactions on medical imaging*, vol. 39, no. 6, pp. 1856–1867, 2019.
- [39] M. Tan and Q. Le, "Efficientnet: Rethinking model scaling for convolutional neural networks," in *International conference on machine learning*. PMLR, 2019, pp. 6105–6114.
- [40] C. Li and M. Wand, "Precomputed real-time texture synthesis with markovian generative adversarial networks," in *European conference on computer vision*. Springer, 2016, pp. 702–716.
- [41] J.-Y. Zhu, T. Park, P. Isola, and A. A. Efros, "Unpaired image-to-image translation using cycle-consistent adversarial networks," in *Proceedings of the IEEE international conference on computer vision*, 2017, pp. 2223–2232.
- [42] C. Ledig, L. Theis, F. Huszár, J. Caballero, A. Cunningham, A. Acosta, A. Aitken, A. Tejani, J. Totz, Z. Wang, et al., "Photo-realistic single image super-resolution using a generative adversarial network," in *Proceedings of the IEEE conference on computer vision and pattern recognition*, 2017, pp. 4681–4690.
- [43] I. Gulrajani, F. Ahmed, M. Arjovsky, V. Dumoulin, and A. C. Courville, "Improved training of wasserstein gans," *Advances in neural information processing systems*, vol. 30, 2017.
- [44] E. R. Bartusiak, S. K. Yarlagadda, D. Güera, P. Bestagini, S. Tubaro, F. M. Zhu, and E. J. Delp, "Splicing detection and localization in satellite imagery using conditional gans," in *2019 IEEE Conference on Multimedia Information Processing and Retrieval (MIPR)*. IEEE, 2019, pp. 91–96.

- [45] G. D. Vo and C. Park, "Robust regression for image binarization under heavy noise and nonuniform background," *Pattern Recognition*, vol. 81, pp. 224–239, 2018.
- [46] N. R. Howe, "Document binarization with automatic parameter tuning," *International journal on document analysis and recognition (ijdar)*, vol. 16, pp. 247–258, 2013.
- [47] F. Jia, C. Shi, K. He, C. Wang, and B. Xiao, "Degraded document image binarization using structural symmetry of strokes," *Pattern Recognition*, vol. 74, pp. 225–240, 2018.
- [48] Z. Yang, Y. Xiong, and G. Wu, "Gdb: Gated convolutions-based document binarization," *arXiv preprint arXiv:2302.02073*, 2023.
- [49] W. Xiong, X. Jia, J. Xu, Z. Xiong, M. Liu, and J. Wang, "Historical document image binarization using background estimation and energy minimization," in *2018 24th International Conference on Pattern Recognition (ICPR)*. IEEE, 2018, pp. 3716–3721.
- [50] S. K. Bera, S. Ghosh, S. Bhowmik, R. Sarkar, and M. Nasipuri, "A non-parametric binarization method based on ensemble of clustering algorithms," *Multimedia Tools and Applications*, vol. 80, no. 5, pp. 7653–7673, 2021.
- [51] S. Kang, B. K. Iwana, and S. Uchida, "Complex image processing with less data—document image binarization by integrating multiple pre-trained u-net modules," *Pattern Recognition*, vol. 109, p. 107577, 2021.
- [52] F. Westphal, N. Lavesson, and H. Grahn, "Document image binarization using recurrent neural networks," in *2018 13th IAPR International Workshop on Document Analysis Systems (DAS)*. IEEE, 2018, pp. 263–268.
- [53] J. Guo, C. He, and X. Zhang, "Nonlinear edge-preserving diffusion with adaptive source for document images binarization," *Applied Mathematics and Computation*, vol. 351, pp. 8–22, 2019.
- [54] S. K. Jenni, M. A. Souibgui, Y. Kessentini, and A. Fornés, "Enhance to read better: a multi-task adversarial network for handwritten document image enhancement," *Pattern Recognition*, vol. 123, p. 108370, 2022.
- [55] Y. Akbari, S. Al-Maadeed, and K. Adam, "Binarization of degraded document images using convolutional neural networks and wavelet-based multichannel images," *IEEE Access*, vol. 8, pp. 153 517–153 534, 2020.
- [56] M. A. Souibgui and Y. Kessentini, "De-gan: A conditional generative adversarial network for document enhancement," *IEEE Transactions on Pattern Analysis and Machine Intelligence*, vol. 44, no. 3, pp. 1180–1191, 2020.
- [57] M. O. Tamrin, M. El-Amine Ech-Cherif, and M. Cheriet, "A two-stage unsupervised deep learning framework for degradation removal in ancient documents," in *Pattern Recognition. ICPR International Workshops and Challenges: Virtual Event, January 10-15, 2021, Proceedings, Part VII*. Springer, 2021, pp. 292–303.
- [58] B. Gatos, K. Ntirogiannis, and I. Pratikakis, "Icdar 2009 document image binarization contest (dibco 2009)," in *2009 10th International conference on document analysis and recognition*. IEEE, 2009, pp. 1375–1382.
- [59] I. Pratikakis, B. Gatos, and K. Ntirogiannis, "H-dibco 2010-handwritten document image binarization competition," in *2010 12th International Conference on Frontiers in Handwriting Recognition*. IEEE, 2010, pp. 727–732.
- [60] H. Z. Nafchi, S. M. Ayatollahi, R. F. Moghaddam, and M. Cheriet, "An efficient ground truthing tool for binarization of historical manuscripts," in *2013 12th International Conference on Document Analysis and Recognition*. IEEE, 2013, pp. 807–811.
- [61] I. Pratikakis, B. Gatos, and K. Ntirogiannis, "Icfhr 2012 competition on handwritten document image binarization (h-dibco 2012)," in *2012 international conference on frontiers in handwriting recognition*. IEEE, 2012, pp. 817–822.
- [62] F. Deng, Z. Wu, Z. Lu, and M. S. Brown, "Binarizationshop: a user-assisted software suite for converting old documents to black-and-white," in *Proceedings of the 10th annual joint conference on Digital libraries*, 2010, pp. 255–258.
- [63] D. P. Kingma and J. Ba, "Adam: A method for stochastic optimization," *arXiv preprint arXiv:1412.6980*, 2014.
- [64] J. Deng, W. Dong, R. Socher, L.-J. Li, K. Li, and L. Fei-Fei, "Imagenet: A large-scale hierarchical image database," in *2009 IEEE conference on computer vision and pattern recognition*. IEEE, 2009, pp. 248–255.